Derivation and examination of a comprehensive free-space optical interconnect link equation

Novak S. Petrovic*, Christopher J. O'Brien and Aleksandar D. Rakic

School of Information Technology and Electrical Engineering
University of Queensland
St Lucia QLD 4072, Brisbane, Australia

ABSTRACT

Free-space optical interconnects (FSOIs) utilize arrays of vertical-cavity surface emitting lasers (VCSELs), microlenses, and photodetectors to effectively overcome the communication bottleneck caused by the poor performance of electrical interconnects. We derived a comprehensive FSOI link equation which can be used to determine the interconnect performance parameters, such as the receiver carrier-to-noise ratio. The link equation includes both optical and electrical noise components. The optical noise component is caused mainly by laser beam diffraction. We have simplified the modelling of optical noise by using the recently introduced Mode Expansion Method. The optical noise component strongly depends on the modal content of the incident VCSEL beam. The models used in the literature assume that the cross-sectional profile of the emitted laser beam resembles the fundamental Gaussian mode. Our link equation takes into account the modal structure of a multimode VCSEL beam. We have investigated the FSOI performance and we found that for each merit function there exists a single set of design parameters yielding the optimal performance. We have also found that the presence of higher-order modes negatively affects the performance. Our results show that FSOIs based on multimode VCSELs can be utilized in chip-level interconnects despite increased beam diffraction.

Keywords: free-space optical interconnect, diffraction, modal expansion.

1. INTRODUCTION

Over their lifetime, computers have enjoyed an exponential growth in speed and power, in accordance with Moore's law.[1] A major obstacle preventing this growth from continuing is the limited onboard bandwidth provided by electrical interconnects.[2] The move to low loss copper lines from aluminium and the development of superior interconnect protocols has stretched the lifetime of the these interconnects.[3] However, a long term solution is needed to allow for the bandwidth which will be required in the future. A proposed solution to this communications bottleneck is to introduce optical interconnects, and in particular free-space optical interconnects (FSOIs).[4-7] FSOIs, consisting of arrays of vertical-cavity surface-emitting lasers (VCSELs), microlenses and photodetectors, can be applied to the design of VLSI, switching systems and parallel optoelectronic processing systems.[8] The integration of VCSELs and photodetectors with electronic circuitry will enable the development of high performance optical interconnects featuring low energy consumption, wide bandwidth, high speed and high density.

Free-space optical interconnects (FSOIs) are well suited for chip and board-level interconnects and several interconnect architectures based on arrays of VCSELs have been proposed recently.[9-11] However, the continuation of successful deployment of FSOIs strongly depends on further development of accurate and simple design models.[12,13] FSOI modelling is far from trivial, due mainly to the necessity of dealing with their electrical and optical characteristics simultaneously.

In this paper we derive a comprehensive FSOI link equation which can be used to quickly and accurately determine the FSOI performance parameters, such as: receiver carrier-to-noise ratio (CNR), bit-error rate (BER), and the space-bandwidth product (SBP). Our link equation includes both optical and electrical noise components. While modelling the

* novak@itee.uq.edu.au

Photonics: Design, Technology, and Packaging, edited by Chennupati Jagadish, Kent D. Choquette, Benjamin J. Eggleton, Brett D. Nener, Keith A. Nugent, Proc. of SPIE Vol. 5277 (SPIE, Bellingham, WA, 2004) · 0277-786X/04/$15 · doi: 10.1117/12.522862

electrical noise component is relatively easy, the generally cumbersome modelling of optical noise was simplified by using the recently introduced Mode Expansion Method (MEM).[13] The optical noise component is caused mainly by laser beam diffraction due to propagation and interaction with optical elements. The optical noise component strongly depends on the modal content of the incident VCSEL beam. The models used in the literature assume that the cross-sectional profile of the emitted laser beam resembles the fundamental Gaussian mode.[12-15] Our FSOI link equation takes into account the modal structure of a multimode VCSEL beam.

We have investigated the FSOI performance based on our model and relative to a number of merit functions, including maximum SBP and interconnect distance. All laser parameters used in the model were measured experimentally and the experimental procedures and results are also presented. We found that for each merit function there exists a single set of design parameters yielding the optimal performance. We have also found that the presence of higher-order modes negatively affects the interconnect performance. Our results show that FSOIs based on multimode VCSELs can be utilized in chip-level interconnects despite increased beam diffraction.

2. FREE-SPACE OPTICAL INTERCONNECT MODEL

Schematic diagram of our free-space optical interconnect is shown in Fig. 1.

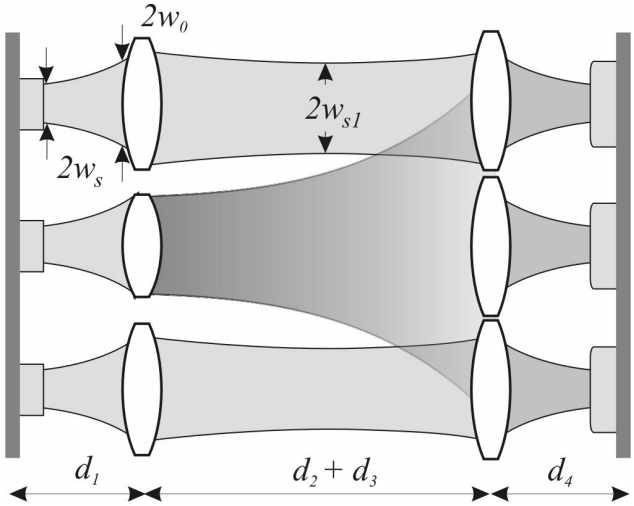

Figure 1: Schematic diagram of the FSOI model.

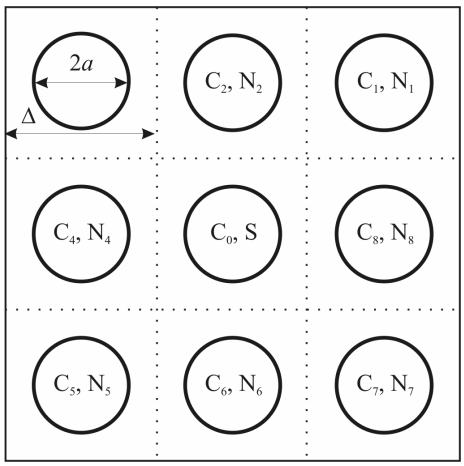

Figure 2: Schematic diagram of the transmitter and receiver microlens arrays.

Three elements of a 2D VCSEL array are shown in Fig. 1 on the left-hand side; the middle (central) channel is taken as the representative communication channel. In each channel the information carrier (VCSEL laser beam) propagates from its beam waist w_s, located at $z = z_s = 0$, to the transmitter microlens, by which it is imaged to its intermediate beam waist w_{s1}. From the intermediate beam waist the beam travels to the receiver microlens which focuses it onto the photodetector. At each microlens plane the beam radius is be larger than the immediately-preceding beam waist. At the transmitter microlens, the beam radius, w_0, is larger than the starting beam waist w_s, due to diffractive spreading of laser beams during propagation. At the receiver microlens the beam radius is larger than the intermediate beam waist w_{s1} due to both diffractive spreading and laser beam diffraction at the aperture of the transmitter microlens. In both cases the result is that the beam lateral extent is such that a portion of the beam will spill out of its designated channel and into the immediately surrounding ones. The portion of carrier power that trespasses will not only not reach the intended photodetector, but it will be detected as optical noise by the neighbouring photodetectors. We distinguish between the optical noise introduced at the transmitter microlens plane (known as the stray-light noise), and the optical noise introduced at the receiver microlens plane (the optical crosstalk noise, OCN). The stray-light noise is much lower than

the OCN and will be neglected. While in Fig. 1 only the central-channel OCN is illustrated – the situation is exactly the same for all neighbouring channels.

Figure 2 shows a portion of the cross-sectional area of the 2D transmitter and receiver microlens planes (assumed to be identical). The central channel is denoted by C_0 while the immediately neighbouring channels are denoted by C_1, …, C_8. The distance between channels is the pitch Δ, while the radius of the microlens apertures is a. The ratio between the aperture diameter and the pitch is known as the fill factor β, $\beta = 2a/\Delta$. In Fig. 1 we have shown how a portion of the carrier power from the central channel contributes to OCN in neighbouring channels. However, in order to calculate the performance of the central channel, we need to know the amount of OCN introduced into C_0 from C_1, …, C_8. Due to the symmetry of the system we see that the OCN from C_0 into C_1, …, C_8 is the same as the noise introduced from C_1, …, C_8 into C_0. We have implicitly assumed that OCN only from the immediately surrounding channels affects the performance of C_0. As indicated in Fig. 2, the carrier power that starts off the central laser and ends up at the central photodetector is denoted by S, while the total OCN that is introduced into the central channel is N, and it consists of the crosstalk noise powers from the immediately surrounding channels, N_1, …, N_8. Both S and N can be calculated most effectively by the mode expansion method, as explained further.

So far only the optical characteristics of the FSOI have been considered. In order to obtain accurate performance indicators, electrical noise components need to be included. We identify the VCSEL relative intensity noise (RIN), and photodetector and preamplifier noises as the most significant sources of electrical noise. Assuming that the optical and electrical noise components can be added in a straightforward fashion, and remembering that the FSOI of Fig. 1 is an analogue system, the carrier-to-noise ratio for its central channel, Ω, can be written as

$$\Omega \equiv \frac{1/2\left(m \cdot R \cdot S\right)^2}{RIN \cdot \left(R \cdot S + R \cdot N\right)^2 B + 2q\left(R \cdot S + R \cdot N + I_d\right)B + \left(4k_B T / R_{eq}\right)BF_t + 1/2\left(m \cdot R \cdot N\right)^2} \tag{1}$$

In the above equation, m represents the analogue modulation index, R is the photodiode responsivity, S represents the portion of the emitted power that is properly detected as the signal power, N represents the portion of the emitted power that is detected as the OCN, RIN is the VCSEL relative intensity noise, B is the receiver bandwidth, I_d is the photodetector dark current, F_t is the preamplifier noise figure, q is the electron charge, k_B is Boltzmann's constant, T is the operating temperature, and R_{eq} is the equivalent resistance of the photodetector load and the preamplifier.

In addition to the CNR, we define more FSOI parameters: the FSOI length and the FSOI density:

$$L \equiv d_1 + d_2 + d_3 + d_4 \approx d_1 + d_2 + d_3\,, \tag{2}$$

$$D \equiv \frac{1}{\Delta^2}\,. \tag{3}$$

Increased interconnection distances L allow greater design flexibility, but result in increased OCN, as laser beam divergence increases with propagation distance. High interconnection density D, measured as the number of channels per unit area, results in increased parallelism and more compact FSOIs. However, larger densities and smaller pitches cause more optical power to incide on neighbouring photodetectors, thus contributing to OCN. Both of these parameters are implicitly contained in Eq. (1) since both S and N depend on L and D.

Very frequently a particular CNR is required. Furthermore, it may also be necessary to compare the performances of several different FSOI configurations, or to compare the performance of a single configuration with different parameters. In order to be able to do that we define another FSOI performance metric, the space-bandwidth product, SBP:

$$SBP \equiv B \times L \times D\,. \tag{4}$$

Given a particular CNR, the SBP gives a measure of the amount of information that can be relayed to each receiver, for each unit of FSOI length and density.

Before Eqs. (1) and (4) can be evaluated, the values of *S* and *N* must be known. *S* and *N* both depend on the FSOI geometry, as well as the modal content of the incident VCSEL beam. If the incident laser beam is represented as a weighted sum of several Hermite-Gaussian laser beam modes:

$$\Psi(x,y,z) = C_{00}\psi_{00}(x,y,z) + C_{01}\psi_{01}(x,y,z) + \ldots + C_{nm}\psi_{nm}(x,y,z). \tag{5}$$

Hermite-Gaussian beams are given by

$$\psi_{nm}(x,y,z) = \sqrt{\frac{1}{2^{n+m-1}\pi(n!)(m!)}}\,\frac{1}{w(z)}\,H_n\!\left(\frac{\sqrt{2}x}{w(z)}\right)H_m\!\left(\frac{\sqrt{2}y}{w(z)}\right)\exp\!\left(\frac{-x^2-y^2}{w^2(z)}\right)\cdot \exp\!\left\{j\left[\frac{k(x^2+y^2)}{2R(z)} - (n+m+1)\arctan\frac{z}{z_R}\right]\right\} \tag{6}$$

where

$$k = \frac{2\pi}{\lambda} \tag{7}$$

$$z_R = \frac{kw_s^2}{2} \tag{8}$$

$$w(z) = w_s\sqrt{1+\left(\frac{z}{z_R}\right)^2} \tag{9}$$

$$R(z) = z\left[1+\left(\frac{z_R}{z}\right)^2\right] \tag{10}$$

where λ is the wavelength of incident laser light, w_s and z_s are laser beam waist size and position respectively, and z_R is the Rayleigh range. $w(z)$ and $R(z)$ represent beam spot size and radius of curvature at position z along the axis of propagation. According to the mode expansion method,[13] the laser beam, imaged and diffracted by the transmitter microlens, is be given as

$$\Psi'(x,y,z) = C'_{00}\,\psi_{00}(x,y,z) + C'_{01}\,\psi_{01}(x,y,z) + \ldots + C'_{NM}\,\psi_{NM}(x,y,z) \tag{11}$$

where the new weighting coefficients are given as

$$\begin{pmatrix} C'_{00} \\ C'_{01} \\ \vdots \\ C'_{NM} \end{pmatrix} = \begin{pmatrix} M_{0000} & M_{0100} & \cdots & M_{nm00} \\ M_{0001} & M_{0101} & \cdots & M_{0001} \\ \vdots & \vdots & \ddots & \vdots \\ M_{00MN} & M_{01MN} & \cdots & M_{nmNM} \end{pmatrix} \begin{pmatrix} C_{00} \\ C_{01} \\ \vdots \\ C_{nm} \end{pmatrix} \tag{12}$$

where

$$M_{nmNM} = \iint_A \psi_{nm}(x_A, y_A, z_A)\left[\psi_{NM}(x_A, y_A, z_A)\right]^* \exp\left[\frac{jk\left(x_A^2 + y_A^2\right)}{2f}\right] dA \tag{13}$$

if $n = N$, and $M_{\mathrm{nmNM}} = 0$ otherwise. A represents the microlens aperture area, the asterisk represents complex conjugation, and f is the microlens focal length. Assuming that all the optical power that falls on each receiver microlens is focussed onto the associated photodetector, it follows that

$$S = \iint_{A_0} \left|\Psi\left(x_{A_0}, y_{A_0}, z_{A_0}\right)\right|^2 dA_0 \tag{14}$$

where A_0 represents the area of the central receiver microlens, and

$$N = \iint_{A_1 \ldots A_8} \left|\Psi\left(x_{A_1 \ldots A_8}, y_{A_1 \ldots A_8}, z_{A_1 \ldots A_8}\right)\right|^2 dA_{A_1 \ldots A_8} \tag{15}$$

where $A_{1\ldots8}$ represents the combined area of the receiver microlenses corresponding to OCN channels C_1, …, C_8. As shall be seen from the experimental procedure outlined in Section 3, when determining the initial laser beam modal composition, we ignore the relative phase difference that may exist between the individual modes, i. e. we assume that

$$C_{nm} = \sqrt{P_{nm}} \tag{16}$$

where P_{nm} represents the measured power in each of the Hermit-Gaussian modes. This approximation makes sense since we are generally interested in the power that is received by each photodetector, and not the shape of the incident field. The variations in power due to initial phase differences are negligible. Finally, given that the initial laser beam consists of the first few Hermite-Gaussian modes, such as TEM_{00}, TEM_{10}, TEM_{01}, and TEM_{20}, M in Eq. (7) need not be more than about 12 by 12. About a dozen modes in the effective beam are sufficient to represent diffraction effects.[13]

3. EXPERIMENTAL MEASUREMENT OF PARAMETER VALUES

Laser parameters were measured and extracted from a *Mode* 8085–2020 oxide confined VCSEL. A computer controlled, automated experiment, shown in Fig. 3, was used to measure its modal and power characteristics. Relative intensity noise (RIN) was also measured.

The laser drive current was increased by regular increments and its spectrum taken at each point. In parallel, the beam profile was recorded by a CCD camera. Combining this data, the modal evolution and competition can be examined and the transverse modes identified. A VCSEL's material gain peak and cavity supported modes are intentionally misaligned at low currents, and move relative to each other as drive current increases. The effect is twofold, and can be observed from the spectra shown in Fig. 4:

I. All lasing modes red-shift with increasing current.
II. A power roll off occurs for each mode as its lasing wavelength becomes unaligned with the material gain.

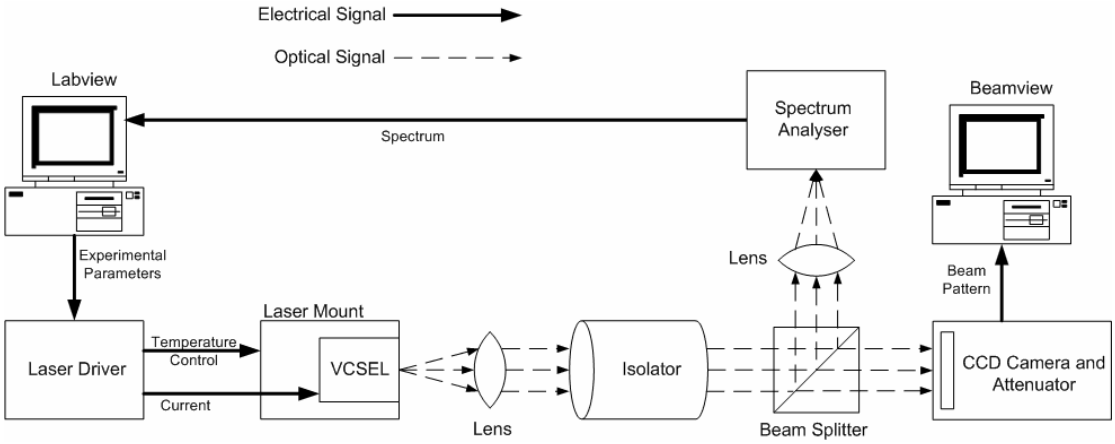

Figure 3: Experimental setup for laser spectrum measurements.

By tracking the lasing mode wavelengths and amplitudes, a modally resolved light-current curve can be constructed, Fig. 5. As the current increases, the dominant fundamental Gaussian mode gives way to a TEM_{10} and TEM_{01} combination, which in turn is replaced by a TEM_{20} mode and other unidentified modes. Modal thresholds can be seen at 3, 6 and 12 mA.

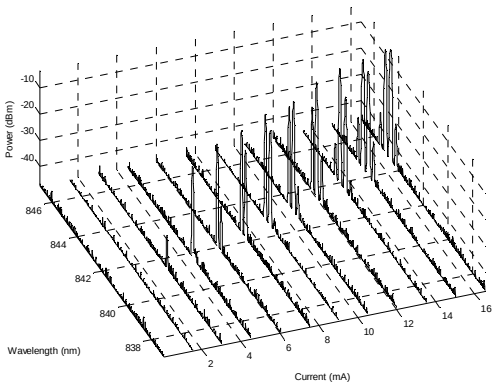

Figure 4: Progression of Spectra

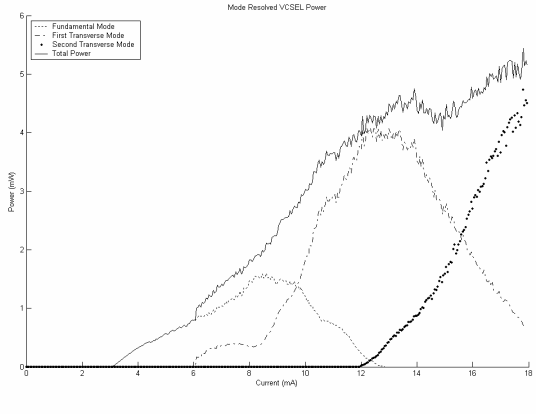

Figure 5: Modally resolved light-current curve

Fluctuations in photon density, caused primarily by spontaneous emission, result in an imperfect laser output[16]. The presence of this noise reduces the data transmission rate which can be achieved without errors, and is termed the Relative Intensity Noise.

$$RIN(\omega) = \frac{P_{AC}(\omega)}{P_{DC} \cdot G(\omega)} \tag{17}$$

Where P_{AC} is the laser's noise component, P_{DC} is the mean optical power and G is the response of the receiver. A tilted optical isolator was used to prevent back reflections into the optical cavity, which adversely affect the RIN measurement. A RIN peak of -127.5 dB/Hz can be observed at the laser's relaxation frequency, 2.8 GHz.

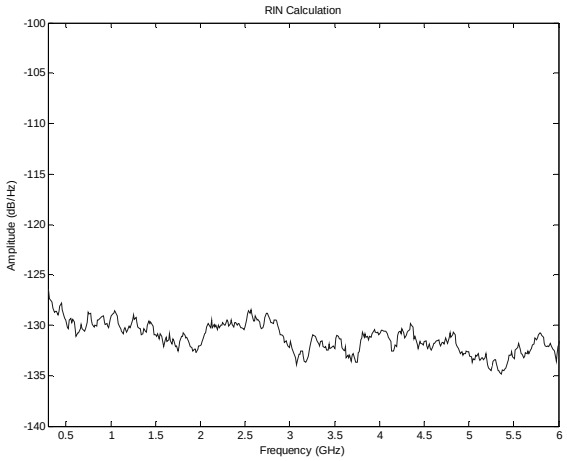

Figure 6: Relative Intensity Noise at 12 mA

4. RESULTS AND DISCUSSION

All parameters used in simulations are shown in Table 1. Regime A in Table 1 denotes the case in which all VCSEL output power is assumed to be in the fundamental TEM_{00} mode, while Regime B considers the measured modal distribution of power.

Name	***Value***	
Wavelength	$\lambda = 850$ nm	
Beam Waist	$w_s = 3$ μm	
Beam Position	$z_s = 0$	
Focal Length	$f = 800$ μm	
Microlens Fill Factor	$\beta = 0.95$ (95 %)	
Microlens Input Distance	$d_1 = f$ + Rayleigh Range ≈ 833 μm	
Modulation Index	$m = 0.25$	
Photodiode Responsivity	$R = 0.6$ A/W	
Relative Intensity Noise	$RIN = -127.5$ dB/Hz	
Receiver Bandwidth	$B = 1$ GHz	
Electron Charge	$q = 1.60218\ 10^{-19}$ C	
Photodiode Dark Current	$I_d = 10$ nA	
Boltzmann's Constant	$k_B = 1.3807\ 10^{-23}$ J/K	
Operating Temperature	$T = 290$ K	
Equivalent Resistance of Photodetector Load and Preamplifier	$R_{eq} = 50\ \Omega$	
Preamplifier Noise Figure	$F_t = 3$ dB	
	Regime A	**Regime B**
VCSEL Bias Current	N/A	$I = 12.6$ mA
Total VCSEL Output Power	$P = 1.7$ mW	$P = 1.7$ mW
VCSEL Output Power in Each Mode	$TEM_{00} = 1.7$ mW	$TEM_{00} = 0.02$ mW $TEM_{10} = 1.60$ mW $TEM_{20} = 0.08$ mW

Table 1: Parameter values used in simulations.

Having all parameter values fixed, the FSOI design procedure consists of finding the values of the interconnection distance *L* and interconnection density *D* that would result in the desired CNR. Figure 3 shows the behaviour of FSOI CNR vs. interconnection length *L* and density *D*.

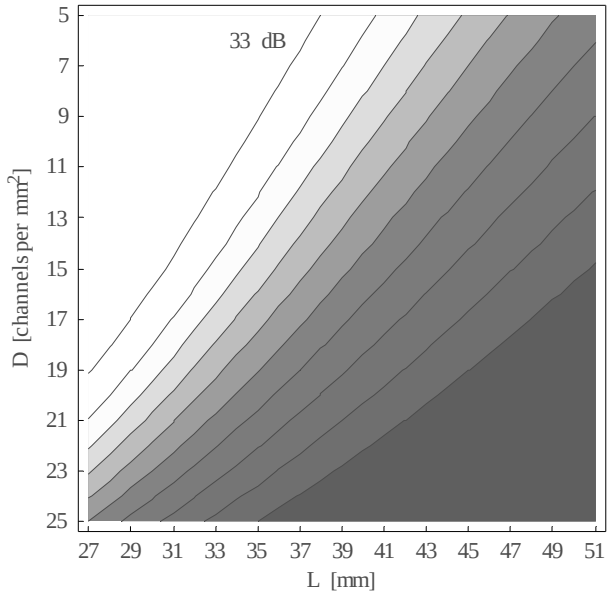

Figure 3: CNR vs. *L* and *D*. The leftmost contour represents CNR of 33 dB and each consecutive contour denotes CNR of 3 dB less. VCSEL is operated in Regime A.

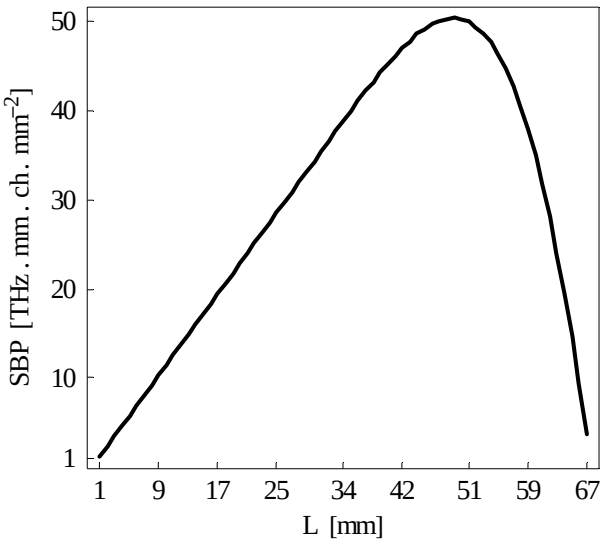

Figure 4: Space-bandwidth product vs. interconnect length *L*. The desired CNR was set to 10 dB, and Δ = 500 μm (D = 4 channels/mm^2). VCSEL is operated in Regime A.

Figure 3 shows that the compromise between *L* and *D* is nearly linear for all CNR values. For a given CNR value, any increase in the interconnection distance must be accompanied by a corresponding decrease in the interconnection density. For example, for CNR = 30 dB, the maximum interconnection density that can be achieved is roughly given by $D \approx -1.23 \cdot L - 54.21$. If *L* is increased by 1 mm, *D* has to be decreased by 1.23 channels/mm^2.

Alternatively, depending on the nature of the FSOI application, we may require a particular value of CNR at the photodetector. Furthermore, the technological aspect may not allow channel densities above a certain value, and the only variable would be the interconnection length *L*. Instead of using the maximum-*L* criterion as in Fig. 3, the interconnect length may be set so as to maximise the space-bandwidth product, SBP. Setting *L* to maximise the SBP would ensure that the FSOI is designed to support the transfer of the maximum amount of information. Figure 4 shows SBP vs. *L*. The maximum SBP occurs at $L \approx 48.7$ mm with the SBP value of about 50.8 THz.mm.channels.mm^{-2}. Note that the interconnection distance is obtained from Fig. 3 in the same case (close to the second-last contour in Fig. 3, for which CNR = 9 dB) would be much greater than 50.8 mm.

Both Figs 3 and 4 were plotted assuming that all laser power was emitted in the fundamental Gaussian mode. We examine the effect of the measured VCSEL multimodal beam structure (Regime B) on CNR and SBP in Figs 5 and 6.

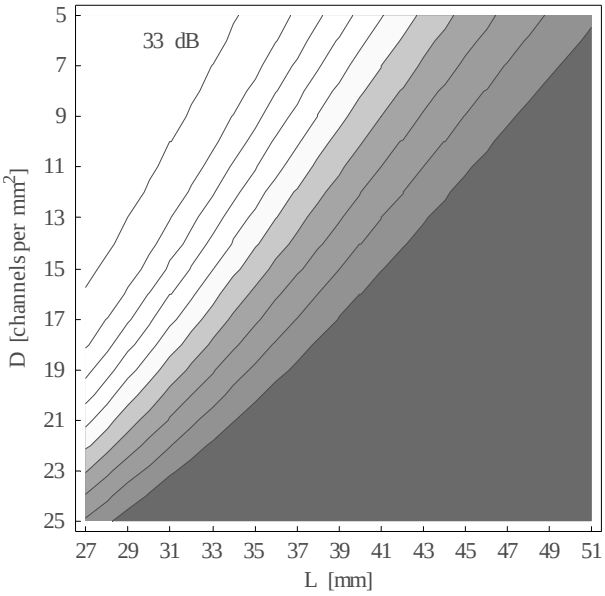

Figure 5: CNR vs. *L* and *D*. The leftmost contour represents CNR of 33 dB and each consecutive contour denotes CNR of 3 dB less.
VCSEL is operated in Regime B.

Contours in Fig. 5 are shifted up and to the left, compared to the ones of Fig. 3. This indicates that an FSOI with the same CNR can be designed even if the VCSEL emits a multimodal beam, but that the resulting maximum FSOI lengths and densities are much smaller. The compromise between *L* and *D* in the case of a multimode VCSEL beam, for the same value of CNR, is still roughly linear as in Fig. 3. However, the slope is much greater in Regime B, indicating that a higher price in density needs to be paid for an increase in interconnect length. For CNR = 30 dB, the maximum interconnection density that can be achieved is approximated by $D \approx -1.44 \cdot L - 56.88$. If *L* is increased by 1 mm, *D* has to be decreased by 1.44 channels/mm^2. Finally, equi-CNR contours are much close together in Fig. 5 indicating that an FSOI operating in Regime B is much more sensitive to variances in *L* and *D*.

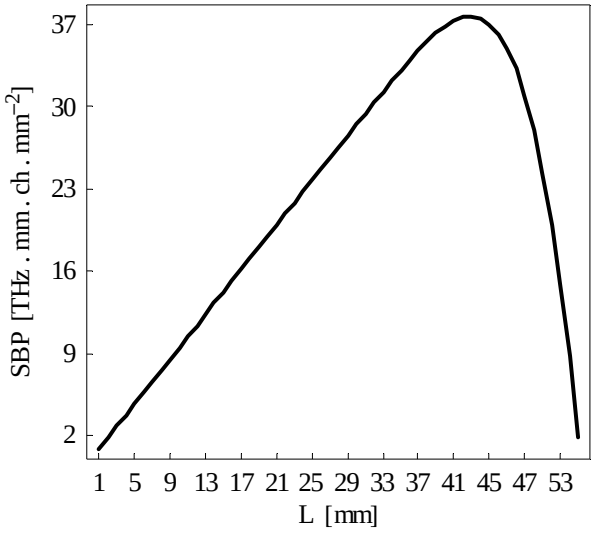

Figure 6: Space-bandwidth product vs. interconnect length *L*.
The desired CNR was set to 10 dB, and Δ = 500 μm (D = 4 channels/mm^2).
VCSEL is operated in Regime B.

Figure 6 shows SBP vs. L in the case of Regime B operation. The maximum SBP occurs at $L \approx 42.6$ mm and SBP $\approx$ 37.9 THz.mm.channels.mm^{-2}. The maximum space-bandwidth product has decreased significantly, indicating that a multimodal VCSEL beam reduces the FSOI information-carrying capacity.

5. CONCLUSION

Continuation of successful deployment of FSOIs strongly depends on further development of accurate and simple design models. We have derived and presented a comprehensive FSOI link equation in which both electrical and optical performance characteristics are included. By using experimentally measured VCSEL parameters, we have found that, in order to obtain a receiver CNR of about 33 dB, the maximum interconnection length achievable is about 30 mm, while the maximum interconnection density is about 10 channels/mm^2. We have found that the multimodal nature of the VCSEL beam leads to: decrease in maximum FSOI lengths and densities for the same CNR, greater sensitivity of CNR to changes in length or density, and greater penalties for readjusting the length-density pair given a particular CNR value. In both cases we were able to find a set of parameter values that maximise SBP. Even though the FSOI information-carrying capability is reduced in the case of a multimodal laser beam, it is still appropriate for many practical applications.

REFERENCES

1. G. E. Moore, "Cramming more components onto integrated circuits," Proceedings of the IEEE, **86**, 82-85, 1998.
2. R. H. Havemann and J. A. Hutchby, "High-performance interconnects: An integration overview," Proceedings of the IEEE, **89**, 586-600, 2001.
3. M. Forbes, J. Gourlay and M. Desmulliez, "Optically interconnected electronic chips: A tutorial and review of the technology," Electronics and Communication Engineering Journal, 221-231, October 2001.
4. D. A. B. Miller, "Optical interconnects to silicon," IEEE Journal on Selected Topics in Quantum Electronics, **6**, 1312-1317, 2000.
5. D. A. B. Miller, "Rationale and challenges for optical interconnects to electronic chips," Proceedings of the IEEE, **88**, 728-749, 2000.
6. R. Wang, A. D. Rakic and M. L. Majewski, "Analysis of lensless free-space optical interconnects based on multi-transverse mode vertical-cavity surface-emitting lasers," Optics Communications, **167**, 261-271, 1999.
7. R. Wang, A. D. Rakic and M. L. Majewski, "Design of microchannel free-space optical interconnects based on vertical-cavity surface-emitting laser arrays," Applied Optics, **41**, 3469-3478, 2002.
8. A. F. J. Levi, "Optical interconnects in systems," Proceedings of the IEEE, **88**, 750-757, 2000.
9. H. M. Ozaktas and M. F. Erden, "Comparison of fully three-dimensional optical, normally conducting, and superconducting interconnections," Applied Optics, **38**, 7264-7275, 1999.
10. A. V. Mule, E. N. Glytsis, T. K. Gaylord and J. D. Meindl, "Electrical and optical clock distribution networks for gigascale microprocessors," IEEE Transactions on VLSI Systems, **10**, 582-594, 2002.
11. N. McArdle, M. Naruse and M. Ishikawa, "Optoelectronic parallel computing using optically interconnected pipelined processing arrays," IEEE Journal of Selected Topics in Quantum Electronics, **5**, 250-260, 1999.
12. S. Tang, R. T. Chen, L. Garrett, D. Gerold and M. M. Li, "Design limitations of highly parallel free-space optical interconnects based on arrays of vertical cavity surface-emitting laser diodes, microlenses and photodetectors, Journal of Lightwave Technology, **12**, 1971-1975, 1994.
13. N. S. Petrovic and A. D. Rakic, "Modelling diffraction in free-space optical interconnects by the mode expansion method," Applied Optics, **42**, 5308-5318, 2003.
14. R. K. Kostuk, "Simulation of board-level free-space optical interconnects for electronic processing," Applied Optics, **31**, 2438-2445, 1992.
15. A. Louri and M. C. Major, "Generalized methodology for modeling and simulating optical interconnection networks using diffraction analysis," Applied Optics, **34**, 4052-4064, 1995.
16. K. Petermann, "Laser Diode Modulation and Noise." Tokyo: KTK Scientific Publishers, 1991.